communications physics

ARTICLE

https://doi.org/10.1038/s42005-023-01297-8 OPEN

Limits of the phonon quasi-particle picture at the cubic-to-tetragonal phase transition in halide perovskites

Erik Fransson[1], Petter Rosander[1], Fredrik Eriksson[1], J. Magnus Rahm[1], Terumasa Tadano[2] & Paul Erhart[1]✉

The soft modes associated with continuous-order phase transitions are associated with strong anharmonicity. This leads to the overdamped limit where the phonon quasi-particle picture can break down. However, this limit is commonly restricted to a narrow temperature range, making it difficult to observe its signature feature, namely the breakdown of the inverse relationship between the relaxation time and damping. Here we present a physically intuitive picture based on the relaxation times of the mode coordinate and its conjugate momentum, which at the instability approach infinity and the inverse damping factor, respectively. We demonstrate this behavior for the cubic-to-tetragonal phase transition of the inorganic halide perovskite $CsPbBr_3$ via molecular dynamics simulations, and show that the overdamped region extends almost 200 K above the transition temperature. Further, we investigate how the dynamics of these soft phonon modes change when crossing the phase transition.

[1] Department of Physics, Chalmers University of Technology, SE-41296 Gothenburg, Sweden. [2] Research Center for Magnetic and Spintronic Materials, National Institute for Materials Science (NIMS), 1-2-1 Sengen, Tsukuba, Ibaraki 305-0047, Japan. ✉email: erhart@chalmers.se

The vibrational properties of solids are pivotal for many physical phenomena, including but not limited to phase stability and thermal conduction. In crystalline solids, the vibrational spectrum is commonly described in terms of phonons as quasi-particle representations of the lattice vibrations. The phonon frequency ω_0 is typically much larger than the damping Γ, and the phonon relaxation time $\tau = 2/\Gamma$ is thus much longer than the oscillation period, such that the quasi-particle picture is well motivated[1–6]. In this so-called underdamped limit, the relaxation time *decreases* as the damping Γ increases.

By comparison, there are far fewer cases when phonon modes become overdamped, i.e., $\omega_0\tau < 1$[7,8]. This can occur either due to large damping or for very soft modes, usually in the immediate vicinity of a phase transition, for example, in the case of body-centered cubic Ti[9–11], rotationally disordered 2D materials[12], in ferroelectrics such as $BaTiO_3$[13–17] or in halide perovskites[18,19]. In the overdamped limit, the relaxation time *increases* with increasing damping Γ, which calls into question the picture of a well-defined phonon mode with a frequency and relaxation time. Overdamped phonon dynamics is, however, usually limited to a rather narrow temperature window, and under these circumstances, the inversion of the relationship between relaxation time and damping cannot be readily observed. Here, we demonstrate that the soft phonons modes associated with the phase transitions in the prototypical halide perovskite $CsPbBr_3$ are, however, outstanding manifestations of this exact behavior as the overdamped region extends almost 200 K above the tetragonal-cubic phase transition.

Halide perovskites are promising materials for photovoltaic and optoelectronic applications. Specifically, $CsPbBr_3$ has received a lot of attention in recent years[20]. With increasing temperature, it undergoes phase transitions from an orthorhombic (Pnma) to a tetragonal (P4/mbm) and eventually a cubic phase ($Pm\bar{3}m$)[21–25]. These phase transitions are connected to specific phonon modes and arise due to the tilting of the $PbBr_6$ octahedra, corresponding to phonon modes at the R and M points (Fig. 1a)[26–30]. Experimentally, these modes have been shown to exhibit overdamped characteristics in the vicinity of the phase transitions[18,19,31]. The phase transitions have also been studied from first-principles and via molecular dynamics (MD) simulations; see, e.g., refs. [32–35].

Here, we reveal the dynamics of the octahedral tilt modes in $CsPbBr_3$ over a wide temperature range via MD simulations based on a machine-learned potential (MLP) that achieves close to density functional theory (DFT) accuracy (Supplementary Note S2, Fig. S1)[36,37]. To obtain access to mode-specific dynamics, we project the MD trajectories onto normal modes that are associated with phase transitions in this material. As shown below, this requires both large systems (comprising at least several 10000 atoms) and sufficiently long times scales (~50–100 ns) in order to achieve converged results (see Supplementary Note S7, Fig. S9, and Fig. S8). The DFT data and the MLP models are provided as a Zenodo dataset[38].

Reference data for the construction of the MLP was generated by DFT calculations[39–41] using the strongly constrained and appropriately normed (SCAN) exchange-correlation functional[42] (Supplementary Note S1). Simulations and atomic structures were handled via the ASE[43] and CALORINE packages[44]. The phonon frequencies and relaxation times obtained with the MLP are in good agreement with experimental work for multiple phonon modes (see Fig. S5). In addition, we consider several different self-consistent phonons (SCP) methods[45] as well as

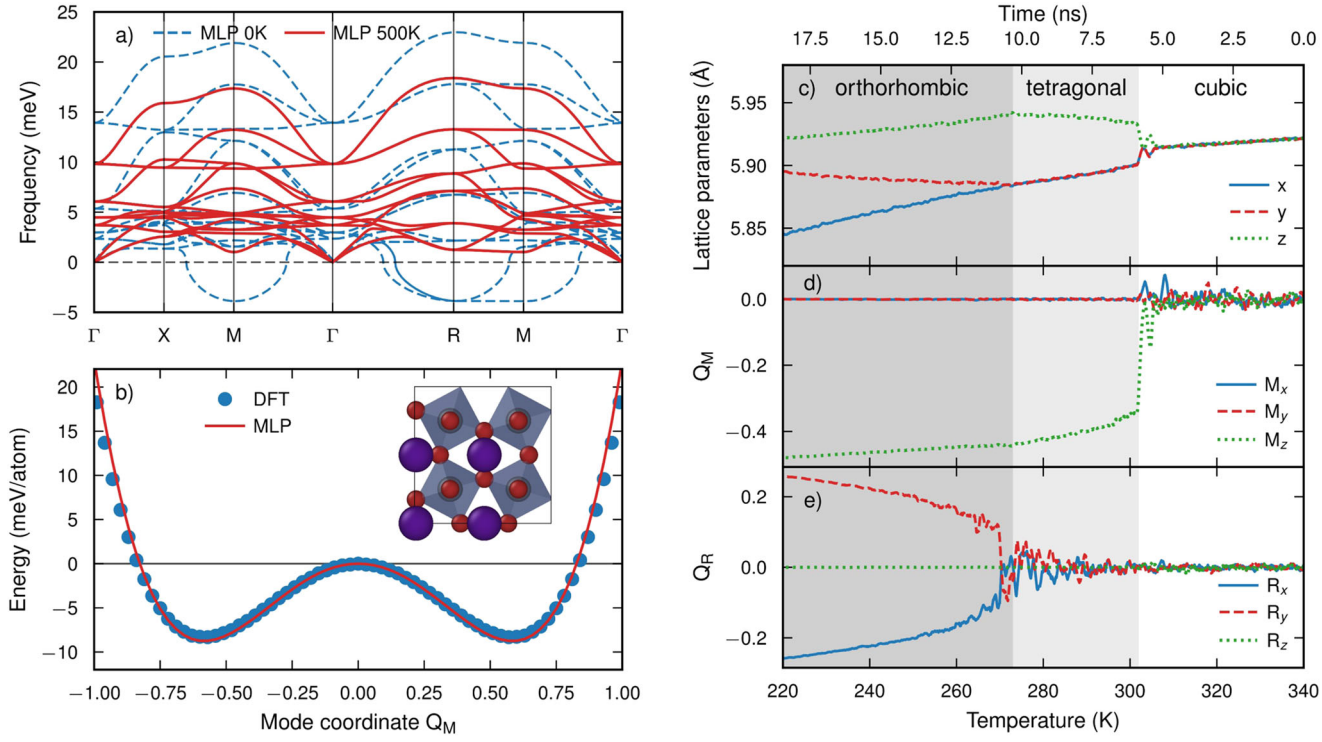

Fig. 1 Phonons and phase transitions in $CsPbBr_3$. a Phonon dispersion for the cubic phases of $CsPbBr_3$ obtained using the machine-learned potential (MLP) in the harmonic approximation, 0 K (dashed lines) and from an effective harmonic model (EHM) at 500 K (solid lines). **b** Potential energy landscape along the unstable M-tilt mode calculated with MLP and density functional theory (DFT). The inset shows the $CsPbBr_3$ crystal structure (Cs purple, Pb gray, Br red) in the energy minima, for which the $PbBr_6$ octahedra have been tilted in-phase (visualization made with OVITO[75]). **c–e** Lattice parameters and mode coordinates obtained from a cooling run based on the isothermal–isobaric (*NpT*) ensemble with phase transitions at approximately 300 K and 275 K. In **c–e** Solid, dashed, and dotted lines refer to the Cartesian directions *x*, *y*, and *z*, respectively.

effective harmonic models (EHMs)[46–49] using the HIPHIVE[50], ALAMODE[51], and SSCHA packages[52].

Results and discussion

Tilt modes and phase transitions. The phase transitions in $CsPbBr_3$, and similarly in many other perovskites, are driven by modes that correspond to tilting of the $PbBr_6$ octahedra. These modes are located at the M (in-phase tilting) and R-points (out-of-phase tilting) in the phonon dispersion for the cubic structure (Fig. 1a). They are threefold degenerate, corresponding to tilting around the three Cartesian directions. These tilt modes exhibit a double-well potential energy surface (PES), which the MLP reproduces perfectly compared to DFT (Fig. 1b).

The MLP predicts temperatures of 300 K and 275 K for the cubic-tetragonal, $T_{c\leftrightarrow t}$, and tetragonal-orthorhombic, $T_{t\leftrightarrow o}$, transitions, respectively (Fig. 1c). This is lower than the experimental values of 400 K and 360 K[20,22,23,25], a discrepancy that can be primarily attributed to the underlying exchange-correlation functional[53].

The mode coordinates of the tilt modes are useful order parameters for analyzing the phase transitions (Fig. 1d, e). At 300 K, the system transitions from the cubic to the tetragonal phase, as seen in both the lattice parameters and in the freezing in of one of the three M-tilt modes (M_z). For the tetragonal phase, two R-modes (R_x and R_y) start to show larger fluctuations, and at 265 K, the system transitions to the orthorhombic phase. Here, we also note the slight difference in character between these two phase transitions. For the cubic-tetragonal transition, the order parameter (Q_M) and lattice parameter change sharply at the transition temperature $T_{c\leftrightarrow t}$ (closer in character to a first-order transition), whereas for the tetragonal-orthorhombic transition, the order parameter and lattice parameter change more gradually around $T_{t\leftrightarrow o}$ (exhibiting continuous character) in agreement with experimental observations of the transition character[20,21]. We note here that the mode coordinate is a global order parameter for the system. In the cubic phase, even though the mode coordinate is on average zero, there still exists a strong local correlation between the neighboring octahedra. This connects to previous work on perovskites regarding the local atomic structure deviating from the cubic structure while globally still appearing cubic[28,29,54–58].

Mode coordinate dynamics. The mode coordinates exhibit interesting dynamical behavior already in the cubic phase far above the transition to the tetragonal phase, which can be conveniently observed in the time domain (Fig. 2a, b). At 500 K, regular (phonon) oscillator behavior is observed, whereas, at 350 K (closer but still above T_C), a slower dynamic component becomes evident. Finally, at 280 K and thus below the phase transition, one observes the common oscillatory motion superimposed on a long timescale hopping motion between the two minima, corresponding to the (degenerate) tetragonal phase (Fig. 1b). We note here that the hopping frequency depends strongly on system size, and is thus not a good thermodynamic observable on its own.

The mode coordinate can be analyzed by fitting the respective autocorrelation functions (ACFs) to a damped harmonic oscillator (DHO) model (Fig. 3). The ACF for a regular (underdamped) mode shows a clear oscillatory pattern, as illustrated here by the highest optical mode at the R-point with a typical relaxation time of about 0.37 ps, which is longer than the mode period of about 0.2 ps (Fig. 3a). The M-tilt mode at 500 K has similar damping but is much softer (yet still underdamped), and the ACF decays with a relaxation time of about 0.58 ps (Fig. 3b). At 350 K (Fig. 3c), however, the same mode is overdamped, and in this case, the DHO model becomes the sum of two exponential decays, see Eq. (3), with relaxation times $\tau_L = 5.22$ ps and $\tau_S = 0.31$ ps. It is interesting to note that the decay time of the ACF at 350 K is about ten times longer than at 500 K. The DHO fits still match the data very well for both the

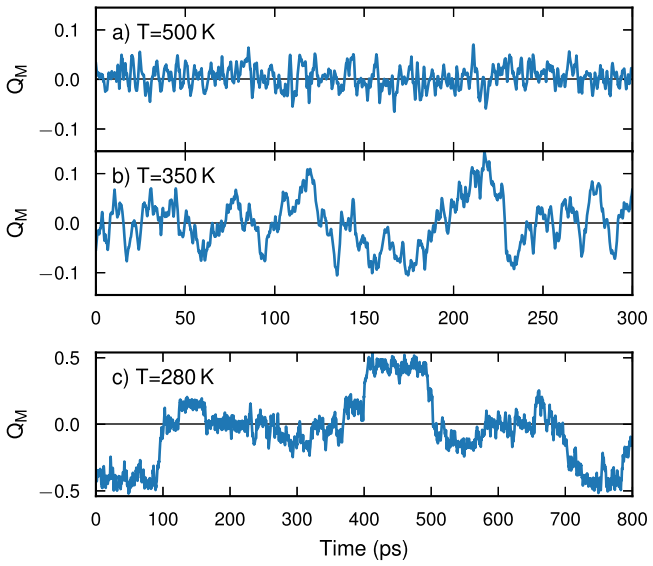

Fig. 2 Phonon mode coordinates. Mode coordinate $Q(t)$ for the M-tilt mode, **a** at 500 K (well above $T_{c\leftrightarrow t}$), **b** at 350 K (close to $T_{c\leftrightarrow t}$), and **c** at 280 K (below above $T_{c\leftrightarrow t}$). The M-tilt mode is three-fold degenerate (x, y, z), but here only the M_z mode is shown. Also note that for 280 K, the system switches the tilt axis at irregular intervals.

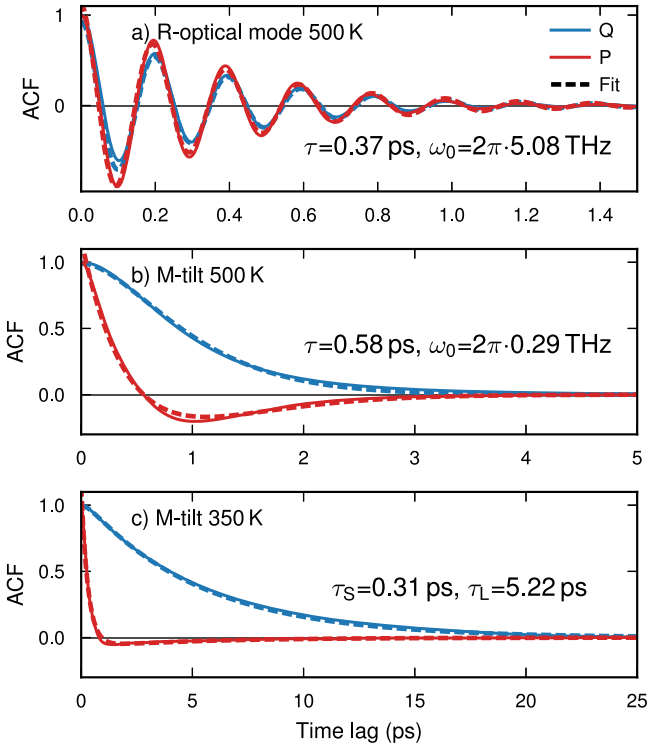

Fig. 3 Phonon mode auto-correlation functions (ACFs). ACFs (solid lines) of **a** the highest optical mode at the R-point as well as the M-tilt mode at **b** 500 K and **c** 350 K, along with fits to a damped harmonic oscillator (DHO) model (dashed lines). Note the large difference in time scale between **b** and **c**.

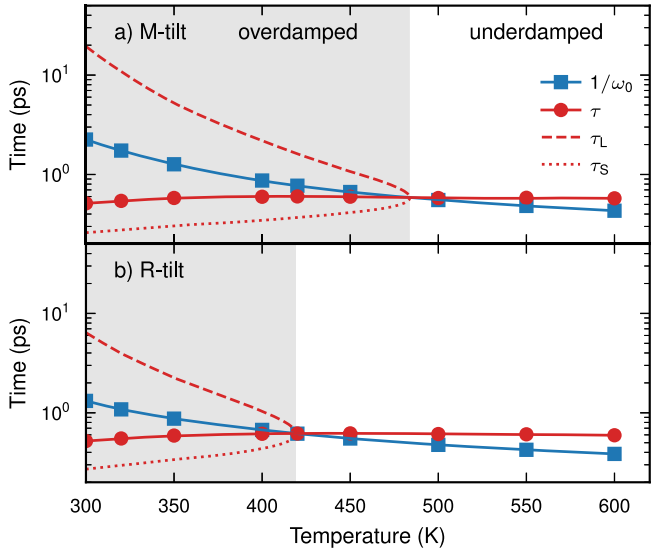

Fig. 4 Phonon frequencies and relaxation times. Frequencies and relaxation times were obtained from auto-correlation functions of **a** M-tilt and **b** R-tilt modes as a function of temperature. The shaded region indicates the overdamped regime. Note that the M-tilt mode is overdamped already about 200 K above the phase transition temperature. Here, markers are data points, and lines are interpolations to guide the eye.

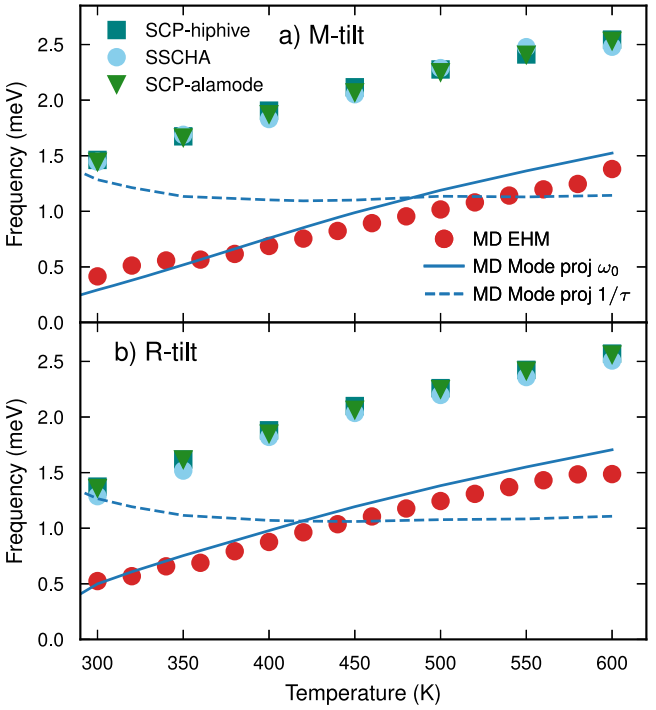

Fig. 5 Phonon frequencies comparison with SCP. Frequencies of **a** M-tilt and **b** R-tilt modes as a function of temperature from several self-consistent phonons (SCP) schemes, effective harmonic models (EHMs) based on molecular dynamics (MD), and damped harmonic oscillator (DHO) frequencies fitted to auto-correlation functions.

underdamped and overdamped cases (see Fig. S11 for how the two exponential decays behave for Q and P in the overdamped case).

When Γ/ω_0 increases, and the system becomes overdamped, the dynamics of the modes are moving towards the diffusive Brownian motion regime. For overdamped modes, the relaxation time of the ACF increases as Γ/ω_0 increases, opposite to the underdamped behavior. While this is a well-known feature of a simple one-dimensional DHO, here, one observes this behavior for phonon modes in a complex atomistic system. This phenomenon arises due to the *free* energy landscape being very flat close to the transition, resembling a bathtub. As a result of the high friction and weak restoring force, it, therefore, takes a long time for the DHO to move back and forth around zero (Fig. 2c; see Fig. S12 for the power spectra)[59].

Frequency and relaxation times vs. temperature. The frequencies and relaxation times of the M-tilt and R-tilt modes are summarized as a function of temperature in Fig. 4. The frequency ω_0 softens significantly with decreasing temperature for both modes, whereas the relaxation time τ is more or less constant. The softening of the frequency thus drives the modes to the overdamped limit with decreasing temperature. The M-tilt and R-tilt modes only become underdamped above 480 K and 410 K, respectively, well above the transition temperature to the tetragonal phase at 300 K. This indicates that we expect the phonon quasi-particle for these modes to work better at high temperatures, which interestingly is the opposite behavior compared to most phonon modes which become more damped and anharmonic with increasing temperature. At the cross-over from the underdamped to the overdamped regime, the two-time scales τ_S and τ_L emerge. When approaching $T_{c\leftrightarrow t}$, we see that τ_L increases exponentially, whereas $\tau_S \to \tau/2$.

SCPs and effective harmonic models. Next, we analyze the representation of these strongly anharmonic modes by commonly used phonon renormalization techniques, specifically different SCP schemes and EHMs (Fig. 5) (see Supplementary Note S5 and Supplementary Note S6 for a more detailed description of the methods). To this end, we constructed 4th-order force constant potentials (FCPs) at each temperature which were used as input to all SCP methods; see Supplementary Note S4 and Fig. S6 for more details. There are several SCPs variants[45]. In SCP-alamode, the Green's function approach is employed as implemented in the ALAMODE package[51]. In the stochastic self-consistent harmonic approximation (SSCHA) scheme, the harmonic free energy is minimized using gradient methods, as implemented in the SSCHA package[52]. In SCP-hiphive second-order force-constants are obtained by iterative fitting to forces from displacements sampled from the harmonic model and forces obtained from the MLP as implemented in the HIPHIVE package[50]. Here, we employ the "bare" SCP implementations in ALAMODE and SSCHA. We note, however, that there are computationally more demanding corrections for both methods[35,60], the analysis of which is, however, beyond the scope of the present work. The EHMs (in this field also referred to as temperature-dependent potentials) are constructed from fitting second-order force constants to displacement and force data obtained from MD simulations with the MLP (see Supplementary Note S6 for details).

Here, we find very similar behavior for both M-tilt and R-tilt modes. The three SCP methods (SCP-hiphive, SSCHA, SCP-alamode) employed here are in excellent agreement with each other, given the differences in theory and implementation between them. The SCP frequencies systematically overestimate the frequency ω_0 obtained from the ACFs by about 1 meV (see Supplementary Note S5 for a more detailed description of the SCP methods). The EHMs constructed by fitting the forces from MD trajectories, on the other hand, show good agreement with the mode projection results. We note here that the trend for SCPs and EHMs to over and underestimate frequencies, respectively, appears to hold for all modes in the system, which is in line with previous studies[35,61–63]. However, while EHMs from MD yield a

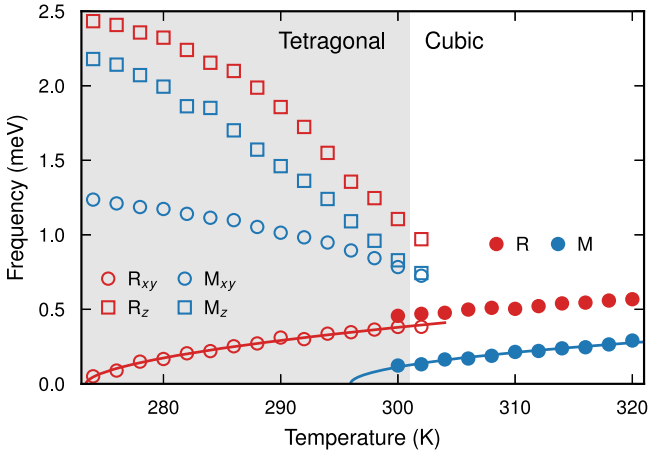

Fig. 6 Phonon frequencies across the phase transition. M and R-tilt mode frequencies from auto-correlation functions and damped harmonic oscillator fits as a function of temperature in the tetragonal and cubic phases. Here, filled symbols correspond to the frequencies in the cubic phase, and open symbols to the frequencies in the tetragonal phase. Solid lines show Curie-Weiss fits of the form, $\omega_0(T) \propto (T - T_C)^p$. For the M-mode in the cubic phase we obtain $T_C = 295$ K (with fixed $p = 0.5$), while for the R_{xy} mode in the tetragonal phase we obtain $T_C = 273$ K and $p = 0.55$. The cubic and tetragonal frequencies overlap in temperature, which is possible due to the first-order character of the transition and the fact that simulations are carried out in the microcanonical (NVE) ensemble, which does not allow for the cell shape to change between cubic and tetragonal.

better frequency for the tilt modes compared to SCP, this is not in general true (see Fig. S7 for details).

Behavior near phase transitions. Next, we look at how these modes behave as the system goes through the transition from the cubic to the tetragonal phase. While in the cubic phase, the three M (and R) modes (denoted with subscripts x, y, and z to indicate the Cartesian direction) are degenerate, the degeneracy is broken in the tetragonal phase, and the z-direction becomes symmetrically distinct from the other two (Fig. 1c, d). Therefore, in order to distinguish these modes, we will denote them by M_{xy} and M_z (analogously for R-modes) in the tetragonal phase. In the tetragonal phase, there exist multiple global minima for the M-mode coordinate, as can be seen in Fig. 2c, where the system jumps between these minima. To avoid capturing this (system-size dependent) hopping time in the ACFs, we employ very large system sizes of up to 400,000 atoms, for which the system remains in the same tetragonal orientation throughout the entire simulation. Furthermore, we extrapolate the frequencies to the infinite system-size limit (Fig. S10).

The resulting frequencies are shown in Fig. 6. For the cubic-to-tetragonal transition, the M-frequency does not go to zero at the transition temperature, which is in agreement with the character of the transition being first order, as observed experimentally[20,21,23]. For the tetragonal-to-orthorhombic phase transition, on the other hand, the R_{xy} frequency does go to zero at the transition temperature, in agreement with a continuous transition as observed experimentally[21]. This leads to the long timescale in the DHO trending to infinity, $\tau_L \to \infty$, as the temperature approaches T_C. Additionally, the R_{xy} mode exhibits a strong size dependence close to the transition temperature (see Fig. S10).

The Curie–Weiss law, $\omega_0(T) \propto (T - T_C)^p$, provides very good fits for the temperature dependence of the modes driving the phase transitions. For the tetragonal-to-orthorhombic transition, the fitted critical temperature, $T_C = 273$ K, agrees very well with the observed transition temperature of 274(1) K, which is consistent with this transition being a continuous transition[21]. Furthermore, the fitted critical exponent of 0.55 is very close to the value of 1/2 suggested by Landau theory observed in many continuous phase transitions driven by soft modes[15,64–66]. The cubic-to-tetragonal transition has a first-order character, as evident from the finite frequency of the M mode at the transition temperature. As a result, fitting both the critical temperature *and* the critical exponent is ambiguous (due to the absence of data at temperatures for which the frequency goes to zero). We, therefore, fix the critical exponent to 1/2, which yields a critical temperature of 295 K, about 7 K lower than the transition temperature. Here, the critical temperature corresponds to the temperature at which the cubic phase becomes dynamically unstable, i.e., the point at which the free energy barrier between the two phases disappears.

The parameter τ remains fairly constant in the tetragonal phase across its entire temperature range for all four modes (Fig. S13). Interestingly, once the M_z mode freezes in (and the tetragonal phase is formed), both the M_z and R_z modes stiffen significantly with temperature. This results in the R_z mode becoming underdamped again with *decreasing* temperature at around 290 K and both M-modes approaching the underdamped limit as the system approaches the orthorhombic transition.

Conclusions

We have carried out a detailed computational analysis of the dynamics in $CsPbBr_3$, focusing in particular on the tilt modes. We observe overdamped modes for the cubic phase almost 200 K above the cubic-to-tetragonal transition temperature. These overdamped tilt-modes exhibit correlation on very long time scales (τ_L) compared to the typical relaxation time (τ) or period ($1/\omega_0$) of the mode. This is in line with the dynamics of the modes transitioning toward Brownian motion due to the frequency approaching zero. What we find here is that these modes can, however, still be mathematically well described as DHOs, which allows one to formally obtain a phonon frequency and relaxation time compliant with a quasi-particle picture. A physically more intuitive description is, however, obtained if the DHO model is described by two relaxation times, which can be approximately associated with mode coordinate and momentum, respectively. As a result of the soft character of these modes, the respective amplitudes can be large already at moderate temperatures. This implies that even for relatively modest electron–phonon coupling strengths, these modes should have a notable impact on the optoelectronic properties of these materials[56,67–70]. A systematic investigation of these effects on a per-mode basis would be an interesting topic of further study.

In addition, we demonstrated that commonly used computational phonon renormalization methods agree very well with each other but, without extensive correction schemes, exhibit systematic errors in describing the frequencies of the anharmonic tilt modes considered here. Understanding the single-point frequencies obtained from such methods and their relation to the full dynamical spectra is thus very important when, e.g., comparing to experimental measurements.

Methods

To analyze phonon modes directly from MD simulations, we employed phonon mode projection[3,71,72]. The MD simulations were carried out using the GPUMD package[37,73]. For more details on the MD simulations, see Supplementary Note S3. The atomic displacements $\boldsymbol{u}(t)$ and velocities $\boldsymbol{v}(t)$ can be projected on a mode λ, with the supercell eigenvector $\boldsymbol{e}_\lambda$ via

$$Q_\lambda(t) = \boldsymbol{u}(t) \cdot \boldsymbol{e}_\lambda \quad \text{and} \quad P_\lambda(t) = \boldsymbol{v}(t) \cdot \boldsymbol{e}_\lambda.$$

Here, the phonon supercell eigenvector of the tilt modes were obtained with PHONOPY[74], and symmetrized such that each of the three degenerate modes corresponds to tilting around the x, y, and z direction respectively. The ACFs of Q and P were calculated in order to analyze the dynamics of the modes of interest as

$$C_Q(t) = \langle Q_\lambda(t')Q_\lambda(t+t')\rangle, \tag{1}$$

which can be modeled as the ACF of a DHO. The DHO is driven by a stochastic force and has a natural frequency ω_0 and a damping Γ. The ACF of the DHO splits into an underdamped regime ($\omega_0 > \Gamma/2$) and an overdamped regime ($\omega_0 < \Gamma/2$). In the underdamped regime, the solution of the DHO is

$$C_Q^{\mathrm{DHO}}(t) = Ae^{-t/\tau}\left(\cos\omega_e t + \frac{\Gamma}{2\omega_e}\sin\omega_e t\right), \tag{2}$$

where $\omega_e = \sqrt{\omega_0^2 - \frac{\Gamma^2}{4}}$, the relaxation time is $\tau = 2/\Gamma$, and A is the amplitude[11]. In the overdamped limit, the solution becomes the sum of two exponential decays as

$$C_Q^{\mathrm{DHO}}(t) = \frac{A}{\tau_{\mathrm{L}} - \tau_{\mathrm{S}}}\left(\tau_{\mathrm{L}}e^{-t/\tau_{\mathrm{L}}} - \tau_{\mathrm{S}}e^{-t/\tau_{\mathrm{S}}}\right) \tag{3}$$

where

$$\tau_{\mathrm{S,L}} = \frac{\tau}{1 \pm \sqrt{1-(\omega_0\tau)^2}}.$$

Here, τ_{S} and τ_{L} denote the short and long timescales, respectively. If the natural frequency approaches zero (e.g., for continuous phase transitions driven by a soft mode), we thus expect $\tau_{\mathrm{L}} \to \infty$ and $\tau_{\mathrm{S}} \to \tau/2$. In this limit, the resulting ACF, $C_Q^{\mathrm{DHO}}(t)$, would only consist of a single exponential decay, with a decay time approaching infinity, which corresponds to the behavior seen in Brownian motion.

Similar expressions are obtained for the ACF of the phonon velocity, which is $C_P^{\mathrm{DHO}}(t) = -\frac{\mathrm{d}^2}{\mathrm{d}t^2}C_Q^{\mathrm{DHO}}(t)$. For the overdamped case, it becomes

$$C_P^{\mathrm{DHO}}(t) = \frac{A}{\tau_{\mathrm{L}} - \tau_{\mathrm{S}}}\left(\frac{1}{\tau_{\mathrm{S}}}e^{-t/\tau_{\mathrm{S}}} - \frac{1}{\tau_{\mathrm{L}}}e^{-t/\tau_{\mathrm{L}}}\right)$$

The ACFs for Q and P were fitted simultaneously to the DHO model in order to extract ω_0 and Γ.

Data availability

The DFT data and the MLP models are provided in a Zenodo dataset[38].

Received: 20 March 2023; Accepted: 3 July 2023;
Published online: 12 July 2023

References

1. Ziman, J. M. *Electrons and Phonons* (Oxford University Press, London, 1960).
2. Sun, T. & Allen, P. B. Lattice thermal conductivity: computations and theory of the high-temperature breakdown of the phonon-gas model. *Phys. Rev. B* **82**, 224305 (2010).
3. Sun, T., Shen, X. & Allen, P. B. Phonon quasiparticles and anharmonic perturbation theory tested by molecular dynamics on a model system. *Phys. Rev. B* **82**, 224304 (2010).
4. Zhang, D.-B., Sun, T. & Wentzcovitch, R. M. Phonon quasiparticles and anharmonic free energy in complex systems. *Phys. Rev. Lett.* **112**, 058501 (2014).
5. Lv, W. & Henry, A. Examining the validity of the phonon gas model in amorphous materials. *Sci. Rep.* **6**, 37675 (2016).
6. Isaeva, L., Barbalinardo, G., Donadio, D. & Baroni, S. Modeling heat transport in crystals and glasses from a unified lattice-dynamical approach. *Nat. Commun.* **10**, 3853 (2019).
7. Silverman, B. D. Collision-broadened phonon line shape in the overdamped or hydrodynamic regime. *Phys. Rev. B* **9**, 203–208 (1974).
8. Schneider, T. & Stoll, E. Molecular-dynamics study of a three-dimensional one-component model for distortive phase transitions. *Phys. Rev. B* **17**, 1302–1322 (1978).
9. Petry, W. et al. Phonon dispersion of the bcc phase of group-IV metals. I. bcc titanium. *Phys. Rev. B* **43**, 10933–10947 (1991).
10. Fransson, E. & Erhart, P. Defects from phonons: atomic transport by concerted motion in simple crystalline metals. *Acta Materialia* **196**, 770 (2020).
11. Fransson, E., Slabanja, M., Erhart, P. & Wahnström, G. dynasor—a tool for extracting dynamical structure factors and current correlation functions from molecular dynamics simulations. *Adv. Theory Simul.* **4**, 2000240 (2021).
12. Kim, S. E. et al. Extremely anisotropic van der Waals thermal conductors. *Nature* **597**, 660–665 (2021).
13. Nakamura, T. Light scattering studies on soft phonon phase transitions. *Ferroelectrics* **9**, 159–169 (1975).
14. Nakamura, T. Soft phonon in $BaTiO_3$. *Ferroelectrics* **137**, 65–88 (1992).
15. Dove, M. T. Theory of displacive phase transitions in minerals. *Am. Mineral.* **82**, 213–244 (1997).
16. Ehsan, S., Arrigoni, M., Madsen, G. K. H., Blaha, P. & Tröster, A. First-principles self-consistent phonon approach to the study of the vibrational properties and structural phase transition of $BaTiO_3$. *Phys. Rev. B* **103**, 094108 (2021).
17. Verdi, C., Ranalli, L., Franchini, C. & Kresse, G. Quantum paraelectricity and structural phase transitions in strontium titanate beyond density-functional theory. *Phys. Rev. Mater.* **7**, L030801 (2023).
18. Songvilay, M. et al. Common acoustic phonon lifetimes in inorganic and hybrid lead halide perovskites. *Phys. Rev. Mater.* **3**, 093602 (2019).
19. Lanigan-Atkins, T. et al. Two-dimensional overdamped fluctuations of the soft perovskite lattice in $CsPbBr_3$. *Nat. Mater.* **20**, 977–983 (2021).
20. Stoumpos, C. C. et al. Crystal growth of the perovskite semiconductor $CsPbBr_3$: a new material for high-energy radiation detection. *Cryst. Growth Des.* **13**, 2722–2727 (2013).
21. Hirotsu, S., Harada, J., Iizumi, M. & Gesi, K. Structural phase transitions in $CsPbBr_3$. *J. Phys. Soc. Jpn.* **37**, 1393–1398 (1974).
22. Sharma, S., Weiden, N. & Weiss, A. Phase transitions in $CsSnCl_3$ and $CsPbBr_3$ an NMR and NQR study. *Z. Naturforsch. A* **46**, 329–336 (1991).
23. Rodová, M., Brožek, J., Knížek, K. & Nitsch, K. Phase transitions in ternary caesium lead bromide. *J. Therm. Anal. Calorim.* **71**, 667–673 (2003).
24. López, C. A. et al. Crystal structure features of $CsPbBr_3$ perovskite prepared by mechanochemical synthesis. *ACS Omega* **5**, 5931–5938 (2020).
25. Malyshkin, D. et al. New phase transition in $CsPbBr_3$. *Mater. Lett.* **278**, 128458 (2020).
26. Huang, L.-y & Lambrecht, W. R. L. Lattice dynamics in perovskite halides $CsSnX_3$ with x = I, Br, Cl. *Phys. Rev. B* **90**, 195201 (2014).
27. da Silva, E. L., Skelton, J. M., Parker, S. C. & Walsh, A. Phase stability and transformations in the halide perovskite $CsSnI_3$. *Phys. Rev. B* **91**, 144107 (2015).
28. Yang, R. X., Skelton, J. M., da Silva, E. L., Frost, J. M. & Walsh, A. Spontaneous octahedral tilting in the cubic inorganic cesium halide perovskites $CsSnX_3$ and $CsPbX_3$ (X = F, Cl, Br, I). *J. Phys. Chem. Lett.* **8**, 4720–4726 (2017).
29. Klarbring, J. & Simak, S. I. Nature of the octahedral tilting phase transitions in perovskites: a case study of $CaMnO_3$. *Phys. Rev. B* **97**, 024108 (2018).
30. Yang, R. X., Skelton, J. M., da Silva, E. L., Frost, J. M. & Walsh, A. Assessment of dynamic structural instabilities across 24 cubic inorganic halide perovskites. *J. Chem. Phys.* **152**, 024703 (2020).
31. Cohen, A. et al. Diverging expressions of anharmonicity in halide perovskites. *Adv. Mater.* **34**, 2107932 (2022).
32. Klarbring, J. Low-energy paths for octahedral tilting in inorganic halide perovskites. *Phys. Rev. B* **99**, 104105 (2019).
33. Zhu, X., Caicedo-Dávila, S., Gehrmann, C. & Egger, D. A. Probing the disorder inside the cubic unit cell of halide perovskites from first-principles. *ACS Appl. Mater. Interfaces* **14**, 22973–22981 (2022).
34. Lahnsteiner, J. & Bokdam, M. Anharmonic lattice dynamics in large thermodynamic ensembles with machine-learning force fields: $CsPbBr_3$, a phonon liquid with Cs rattlers. *Phys. Rev. B* **105**, 024302 (2022).
35. Tadano, T. & Saidi, W. A. First-principles phonon quasiparticle theory applied to a strongly anharmonic halide perovskite. *Phys. Rev. Lett.* **129**, 185901 (2022).
36. Fan, Z. et al. Neuroevolution machine learning potentials: combining high accuracy and low cost in atomistic simulations and application to heat transport. *Phys. Rev. B* **104**, 104309 (2021).
37. Fan, Z. et al. GPUMD: a package for constructing accurate machine-learned potentials and performing highly efficient atomistic simulations. *J. Chem. Phys.* **157**, 114801 (2022).
38. Zenodo dataset. https://doi.org/10.5281/zenodo.7313503 (2022).
39. Kresse, G. & Hafner, J. Ab initio molecular dynamics for liquid metals. *Phys. Rev. B* **47**, 558–561 (1993).
40. Blöchl, P. E. Projector augmented-wave method. *Phys. Rev. B* **50**, 17953–17979 (1994).
41. Kresse, G. & Furthmüller, J. Efficiency of ab-initio total energy calculations for metals and semiconductors using a plane-wave basis set. *Comput. Mater. Sci.* **6**, 15–50 (1996).
42. Sun, J., Ruzsinszky, A. & Perdew, J. P. Strongly constrained and appropriately normed semilocal density functional. *Phys. Rev. Lett.* **115**, 036402 (2015).
43. Larsen, A. H. et al. The atomic simulation environment—a Python library for working with atoms. *J. Phys.* **29**, 273002 (2017).
44. CALORINE. https://gitlab.com/materials-modeling/calorine Accessed: 2023-02-10 (2022).
45. Esfarjani, K. & Liang, Y. Thermodynamics of anharmonic lattices from first principles. In *Nanoscale Energy Transport*, 2053-2563, 7–1 to 7–35 (IOP Publishing, Bristol England, 2020). https://doi.org/10.1088/978-0-7503-1738-2ch7.
46. Kong, L. T., Bartels, G., Campañá, C., Denniston, C. & Müser, M. H. Implementation of Green's function molecular dynamics: an extension to LAMMPS. *Comput. Phys. Commun.* **180**, 1004–1010 (2009).

47. Kong, L. T. Phonon dispersion measured directly from molecular dynamics simulations. *Comput. Phys. Commun.* **182**, 2201–2207 (2011).
48. Andersson, T. *One-Shot Free Energy Calculations for Crystalline Materials*. Master's thesis. (Chalmers University of Technology, 2012).
49. Hellman, O., Steneteg, P., Abrikosov, I. A. & Simak, S. I. Temperature dependent effective potential method for accurate free energy calculations of solids. *Phys. Rev. B* **87**, 104111 (2013).
50. Eriksson, F., Fransson, E. & Erhart, P. The Hiphive package for the extraction of high-order force constants by machine learning. *Adv. Theory Simul.* **2**, 1800184 (2019).
51. Tadano, T., Gohda, Y. & Tsuneyuki, S. Anharmonic force constants extracted from first-principles molecular dynamics: applications to heat transfer simulations. *J. Phys.* **26**, 225402 (2014).
52. Monacelli, L. et al. The stochastic self-consistent harmonic approximation: calculating vibrational properties of materials with full quantum and anharmonic effects. *J. Phys.* **33**, 363001 (2021).
53. Fransson, E., Wiktor, J. & Erhart, P. Phase transitions in inorganic halide perovskites from machine learning potentials. *J. Phys. Chem. C* https://doi.org/10.1021/acs.jpcc.3c01542 (2023).
54. Fabini, D. H. et al. Dynamic stereochemical activity of the Sn^{2+} lone pair in perovskite $CsSnBr_3$. *J. Am. Chem. Soc.* **138**, 11820–11832 (2016).
55. Bertolotti, F. et al. Coherent nanotwins and dynamic disorder in cesium lead halide perovskite nanocrystals. *ACS Nano* **11**, 3819–3831 (2017).
56. Wiktor, J., Rothlisberger, U. & Pasquarello, A. Predictive determination of band gaps of inorganic halide perovskites. *J. Phys. Chem. Lett.* **8**, 5507–5512 (2017).
57. Levin, I. et al. Nanoscale-correlated octahedral rotations in $BaZrO_3$. *Phys. Rev. B* **104**, 214109 (2021).
58. Malavasi, L. et al. Cubic or not cubic? The short-range order of tin halide perovskites. https://doi.org/10.26434/chemrxiv-2022-3l933 (2022).
59. Volpe, G. & Volpe, G. Simulation of a Brownian particle in an optical trap. *Am. J. Phys.* **81**, 224–230 (2013).
60. Bianco, R., Errea, I., Paulatto, L., Calandra, M. & Mauri, F. Second-order structural phase transitions, free energy curvature, and temperature-dependent anharmonic phonons in the self-consistent harmonic approximation: Theory and stochastic implementation. *Phys. Rev. B* **96**, 014111 (2017).
61. Korotaev, P., Belov, M. & Yanilkin, A. Reproducibility of vibrational free energy by different methods. *Comput. Mater. Sci.* **150**, 47–53 (2018).
62. Metsanurk, E. & Klintenberg, M. Sampling-dependent systematic errors in effective harmonic models. *Phys. Rev. B* **99**, 184304 (2019).
63. Tolborg, K. & Walsh, A. Anharmonic and entropic stabilisation of cubic zirconia from first principles. Preprint at *ChemRxiv* https://doi.org/10.26434/chemrxiv-2022-lkzm9 (2022).
64. Cochran, W. Crystal stability and the theory of ferroelectricity. *Adv. Phys.* **9**, 387–423 (1960).
65. Pytte, E. & Feder, J. Theory of a structural phase transition in perovskite-type crystals. *Phys. Rev.* **187**, 1077–1088 (1969).
66. Scott, J. F. Soft-mode spectroscopy: experimental studies of structural phase transitions. *Rev. Mod. Phys.* **46**, 83–128 (1974).
67. Marronnier, A. et al. Influence of disorder and anharmonic fluctuations on the dynamical rashba effect in purely inorganic lead-halide perovskites. *J. Phys. Chem. C* **123**, 291–298 (2018).
68. Kirchartz, T., Markvart, T., Rau, U. & Egger, D. A. Impact of small phonon energies on the charge-carrier lifetimes in metal-halide perovskites. *J. Phys. Chem. Lett.* **9**, 939–946 (2018).
69. Zhao, X.-G., Dalpian, G. M., Wang, Z. & Zunger, A. Polymorphous nature of cubic halide perovskites. *Phys. Rev. B* **101**, 155137 (2020).
70. Wang, H., Tal, A., Bischoff, T., Gono, P. & Pasquarello, A. Accurate and efficient band-gap predictions for metal halide perovskites at finite temperature. *npj Comput. Mater.* https://doi.org/10.1038/s41524-022-00869-6 (2022).
71. Carreras, A., Togo, A. & Tanaka, I. Dynaphopy: a code for extracting phonon quasiparticles from molecular dynamics simulations. *Comput. Phys. Commun.* **221**, 221–234 (2017).
72. Rohskopf, A., Li, R., Luo, T. & Henry, A. A computational framework for modeling and simulating vibrational mode dynamics. *Model. Simul. Mater. Sci. Eng.* **30**, 045010 (2022).
73. Fan, Z., Chen, W., Vierimaa, V. & Harju, A. Efficient molecular dynamics simulations with many-body potentials on graphics processing units. *Comput. Phys. Commun.* **218**, 10–16 (2017).
74. Togo, A. & Tanaka, I. First principles phonon calculations in materials science. *Scr. Mater.* **108**, 1–5 (2015).
75. Stukowski, A. Visualization and analysis of atomistic simulation data with ovito—the open visualization tool. *Model. Simul. Mater. Sci. Eng.* **18**, 015012 (2009).

Acknowledgements

This work was funded by the Swedish Research Council (grant Nos. 2018-06482, 2020-04935, and 2021-05072), the Swedish Energy Agency (grant No. 45410-1), the Area of Advance Nano at Chalmers, and the Chalmers Initiative for Advancement of Neutron and Synchrotron Techniques. T.T. was supported by JSPS KAKENHI grant No. 21K03424. The computations were enabled by resources provided by the National Academic Infrastructure for Supercomputing in Sweden (NAISS) at NSC, C3SE, and PDC, partially funded by the Swedish Research Council through grant agreement No. 2022-06725.

Author contributions

E.F. carried out the analysis based on MD simulations and wrote the first draft of the paper. P.R. constructed the 4th-order FCPs and carried out the SCP analysis with HIPHIVE and SSCHA, as well as some of the DFT calculations. J.M.R. and P.E. carried out the DFT calculations and J.M.R. trained the neuroevolution potential (NEP) model. F.E. analyzed the DHO expressions. T.T. constructed an interface between HIPHIVE and ALAMODE and carried out the SCP calculations with ALAMODE. P.E. supervised the project. All authors reviewed and edited the paper.

Funding

Open access funding provided by Chalmers University of Technology.

Competing interests

The authors declare no competing interests.

Additional information

Supplementary information The online version contains supplementary material available at https://doi.org/10.1038/s42005-023-01297-8.

Correspondence and requests for materials should be addressed to Paul Erhart.

Peer review information *Communications Physics* thanks Olivier Delaire and the other anonymous reviewer(s) for their contribution to the peer review of this work.

Reprints and permission information is available at http://www.nature.com/reprints

Publisher's note Springer Nature remains neutral with regard to jurisdictional claims in published maps and institutional affiliations.

Supplemental Material:

Limits of the phonon quasi-particle picture at the cubic-to-tetragonal phase transition in halide perovskites

Erik Fransson[1], Petter Rosander[1], Fredrik Eriksson[1], J. Magnus Rahm[1], Terumasa Tadano[2], and Paul Erhart[1]

[1] *Department of Physics, Chalmers University of Technology, SE-41296, Gothenburg, Sweden*
[2] *Research Center for Magnetic and Spintronic Materials, National Institute for Materials Science (NIMS), 1-2-1 Sengen, Tsukuba, Ibaraki 305-0047, Japan*

Contents

Supplementary Notes

Supplementary Note S1: Density functional theory calculations

Density functional theory (DFT) calculations were performed using the projector augmented-wave method[1] as implemented in the Vienna ab-initio simulation package[2,3]. To this end, the exchange-correlation contribution was represented using the strongly constrained and appropriately normed (SCAN) density functional[4]. The Brillouin zone was sampled with a Γ-centered grid with a $\boldsymbol{k}$-point density of 0.25 Å^{-1} and Gaussian smearing with a width of 0.1 eV.

Supplementary Note S2: Training and validation of potential

A neuroevolution potential (NEP) model was fitted with the GPUMD package (version 3.3.1)[5,6]. The NEP is based on a neural network for which local atomic environments are described by smooth overlap of atomic positions (SOAP)-like descriptors[7] defined in Ref.[8], here with radial and angular cutoff of 8 Å and 4 Å, respectively, and radial and angular order 12 and 6, respectively. The neural network consists of one hidden layer of 40 neurons and a hyperbolic tangent activation function and was trained over 210,000 generations using the natural evolution strategy[9] implemented in GPUMD. Both the L_1 and the L_2 norm were regularized using $\lambda_1 = \lambda_2 = 0.02$ (as defined in Ref[6]). The model was fitted to forces, energies and virials from DFT calculation of 642 atomic structures with a total of 176 920 atoms, and validated against a set of 72 structures calculated with a total of 19 800 atoms. These structures were generated by means of active learning, i.e., preliminary models were fitted and new structures extracted from MD simulations based on those models were used to fit an updated model.

The model validation against DFT data can be seen in figures Fig. S1, Fig. S2, Fig. S3, Fig. S4. The energy and lattice parameters of the relevant phases are given in Table S1 In Fig. S5 the obtained phonon dispersion from MDs simulations is compared to experimental work[10,11].

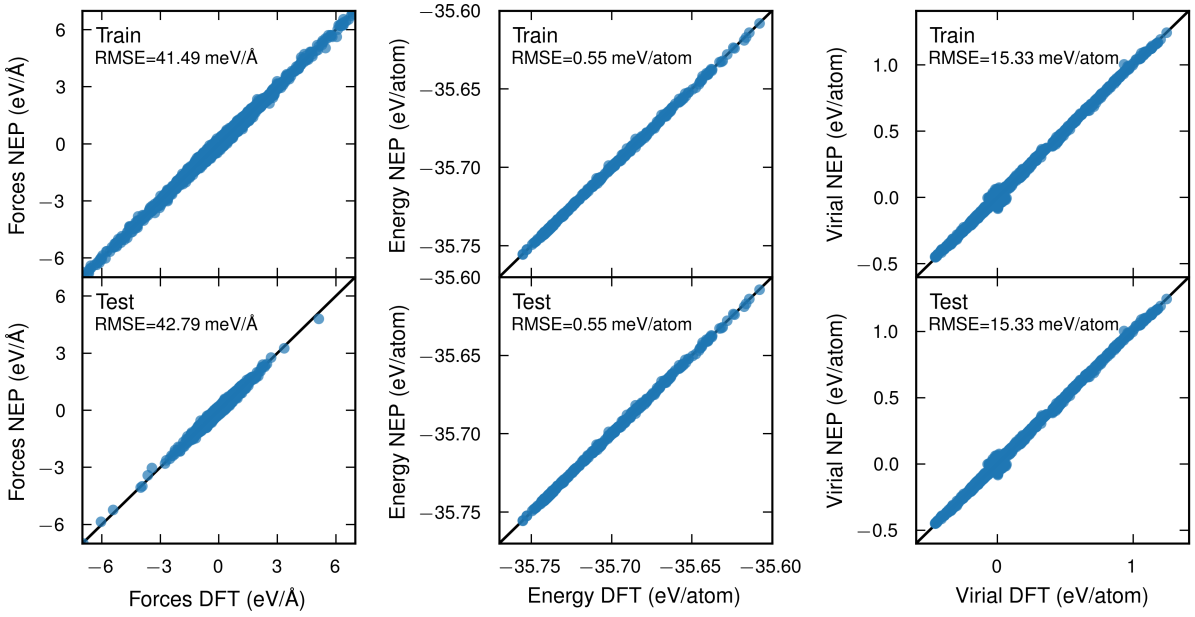

Figure S1: **Parity plots.** Parity plots for energies, forces, and virials for training (top) and test (bottom) data.

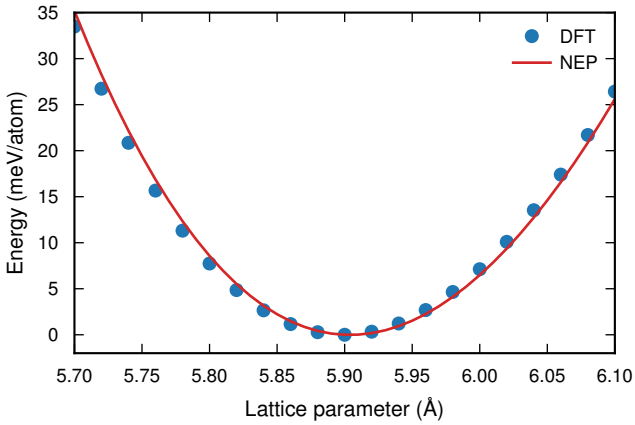

Figure S2: **Energy-volume curves.** Energy-volume curves for the cubic phase of $CsPbBr_3$ from NEP and DFT calculations.

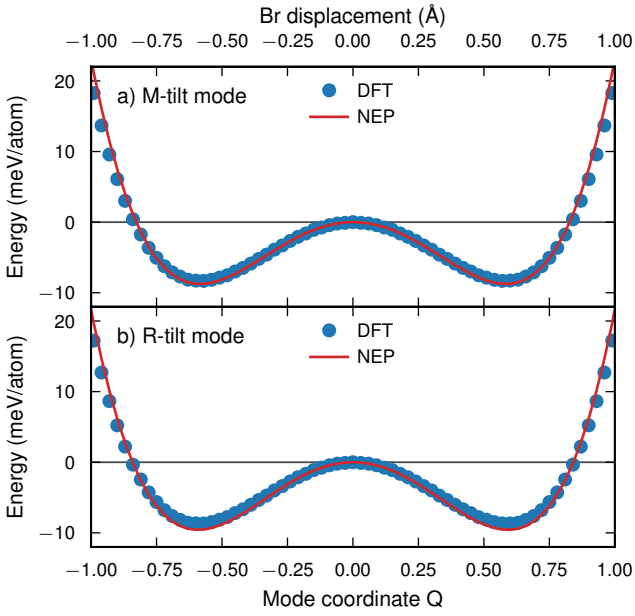

Figure S3: **Energy landscape along phonon modes.** Phonon mode PES along the M and R tilt modes with NEP and DFT. The top x-axis indicates the displacement of each Br atoms involved in the mode in units of Å.

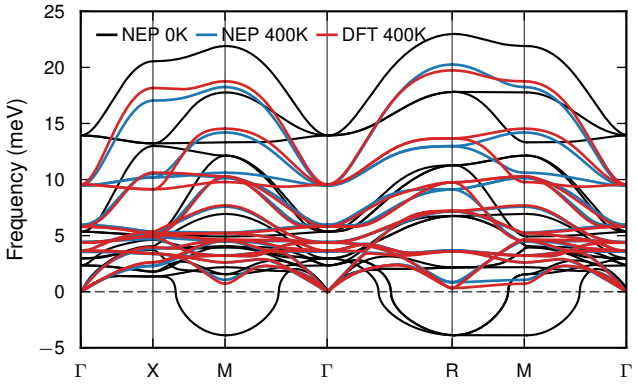

Figure S4: **Phonon dispersion of cubic $CsPbBr_3$.** Phonon dispersions for the cubic phase of $CsPbBr_3$ with the finite temperature dispersions from EHM for DFT and NEP constructed from the same training structures (MD at 400 K).

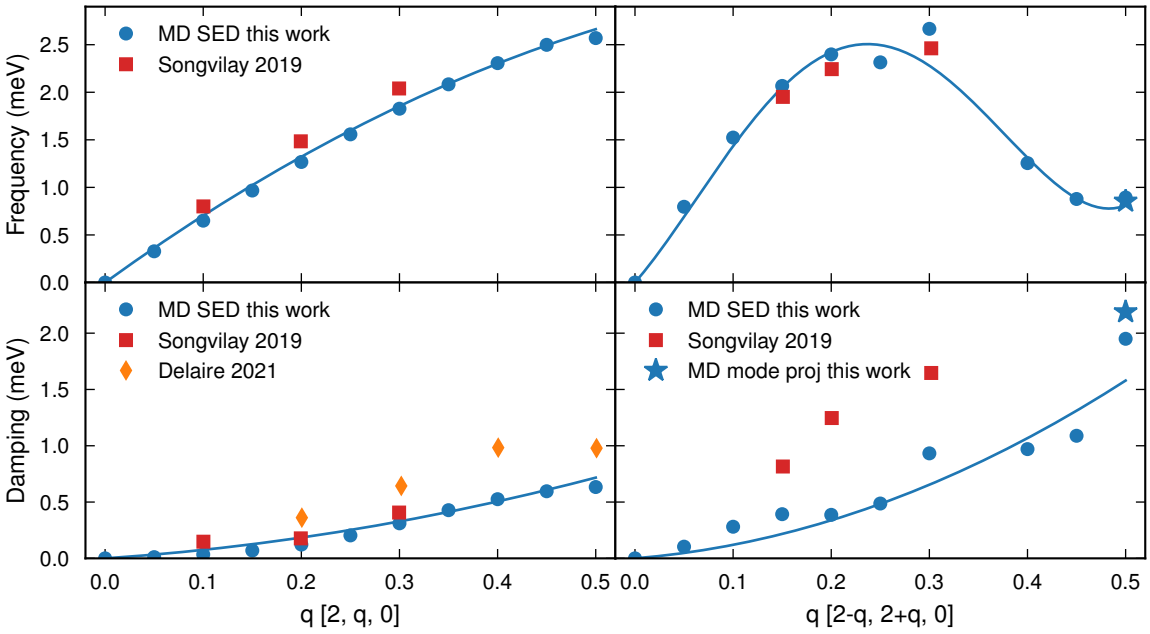

Figure S5: **Phonon dispersion from molecular dynamics compared to experiment.** Phonon frequencies and phonon linewidths for Γ →X (left) and Γ →M (right) calculated using the SED method from MD simulations compared to experimental data [10,11] at 420 K. The point marked with a star correspond to the values obtained through phonon mode-projection. Solid lines serve as guides to the eyes (polynomial fits to the MD data).

Supplementary Note S3: Molecular dynamics details

The phase transitions were studied with simulated annealing simulations in the isothermal-isobaric (NpT) ensemble with a supercell comprising 25 920 atoms. The lattice parameters were extracted for the cubic and tetragonal phases from NpT runs and used in NVT and NVE runs. For all MD simulations a time step of 1 fs was used.

The dynamics of the phonon modes were analyzed via phonon mode projections from MD simulations in the microcanonical (NVE) ensemble with a supercell comprising 8640 atoms ($12 \times 12 \times 12$ conventional cubic cells) see Fig. S9 for size convergence. Close to the cubic-tetragonal transition and for the tetragonal phase (see Fig 6) we used larger system sizes upto 400 000 atoms and used supercell size extrapolation (Fig. S10) in order to achieve converged frequencies. For each temperature a total of 50 independent simulations was carried out, each being 1 ns long. Each simulation was first equilibrated for 100 ps in the NVT ensemble, and then the mode coordinate and velocity, Q and P, were recorded in the NVE ensemble every 10th step. The autocorrelation functions (ACFs) of Q and P were calculated for each MD simulation and then were averaged over the 50 independent runs (see Fig. S8 for convergence test).

Supplementary Note S4: Force constant expansions

The PES can be expanded in a Taylor series in the atomic displacements $\boldsymbol{u}$ relative to a set of reference positions $\boldsymbol{r}_0$

$$U = U_0 + \frac{1}{2}\Phi_{ij}^{\alpha\beta} u_i^\alpha u_j^\beta + \frac{1}{3!}\Phi_{ijk}^{\alpha\beta\gamma} u_i^\alpha u_j^\beta u_k^\gamma + \ldots, \tag{S1}$$

where Φ are the force constants (FCs), Latin indices enumerate atoms, Greek indices enumerate Cartesian coordinates, and the Einstein summation convention applies.

For all self-consistent phonons (SCP) results temperature specific fourth-order force constant potentials (FCPs) were used. These FCPs were trained from MD simulations with the NEP.

Supplementary Note S5: Self-consistent phonons

There are several different variations of SCPs[12]. Here, we employ three variants as implemented in ALAMODE[13], SSCHA[14] and HIPHIVE[15].

The SCP implementation in ALAMODE is based on Green's functions.

In the SSCHA scheme the free energy of the harmonic model is minimized,

$$\min_{\mathcal{H}} \{F_{\mathcal{H}} + \langle V - \mathcal{V} \rangle_{\mathcal{H}}\}, \tag{S2}$$

where $\mathcal{H}$ the harmonic Hamiltonian and H is the anharmonic Hamiltonian. The first term is thus the harmonic free energy, and the second term is the difference between the harmonic and anharmonic potential evaluated in the harmonic ensemble.

In HIPHIVE a force-fitting SCP is implemented as

$$\min_{\mathbf{\Phi}} \left\langle \left(f_i^{\text{har}} - f_i\right)^2 \right\rangle_{\mathcal{H}}, \tag{S3}$$

where f_i^{har} are the harmonic forces that depend on the harmonic FCs $\mathbf{\Phi}$ and f_i are the anharmonic forces. Here, the ensemble average is carried out in the harmonic ensemble, $\mathcal{H}$.

Supplementary Note S6: Effective harmonic models from MD

Phonon renormalization can also be done by constructing EHMs directly from MD simulations by fitting the harmonic FCs to displacement and force data as follows

$$\min_{\mathbf{\Phi}} \left\langle \left(f_i^{\text{har}} - f_i\right)^2 \right\rangle_{H} \tag{S4}$$

This approach has been popularized in the TDEP package[16]. In order to train the EHMs we run MD for a 6×6×6 system in the NVT ensemble (1080 atoms) and select 200 snapshots each separated by 500 fs for each temperature. From these 200 snapshots displacements and forces are extracted and used to fit EHMs with a harmonic cutoff of 9 Å.

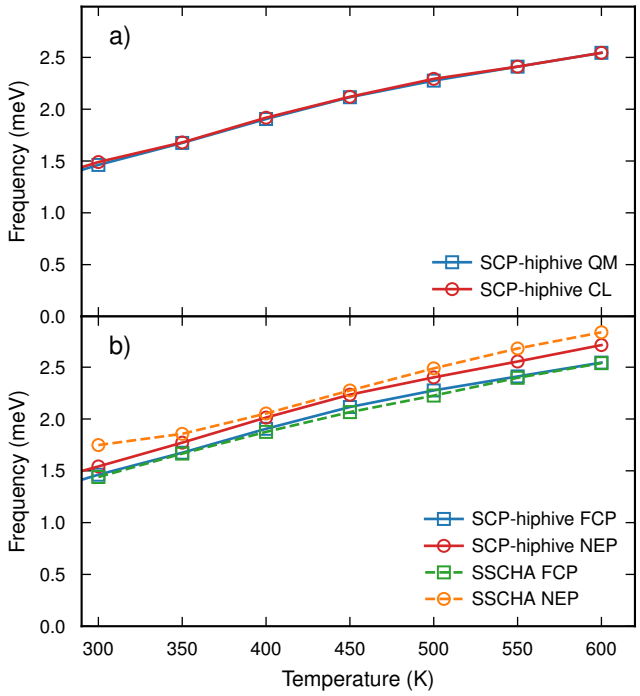

Figure S6: **Self-consistent phonons.** (a) The M-tilt mode frequency vs temperature with the fourth order FCP using SCP-hiphive quantum (QM) and classical (CL) sampling. (b) The M-tilt mode frequency vs temperature with compared between fourth-order FCP and using the NEP model directly.

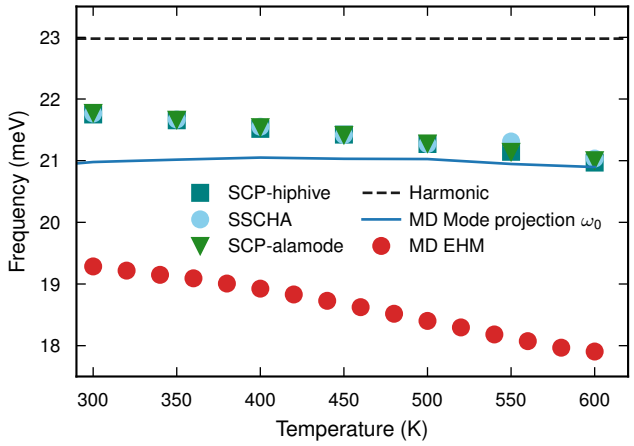

Figure S7: **Frequency of optical mode.** Temperature dependent frequency for the highest optical mode at R with different methods.

Supplementary Note S7: Phonons and mode projections

Below some more details and convergence tests are shown for the phonon mode projections. Convergence with respect to simulation time is shown in Fig. S8 and with respect to system size Fig. S9. The size-extrapolation of the phonon frequency and lifetimes are shown in Fig. S10.

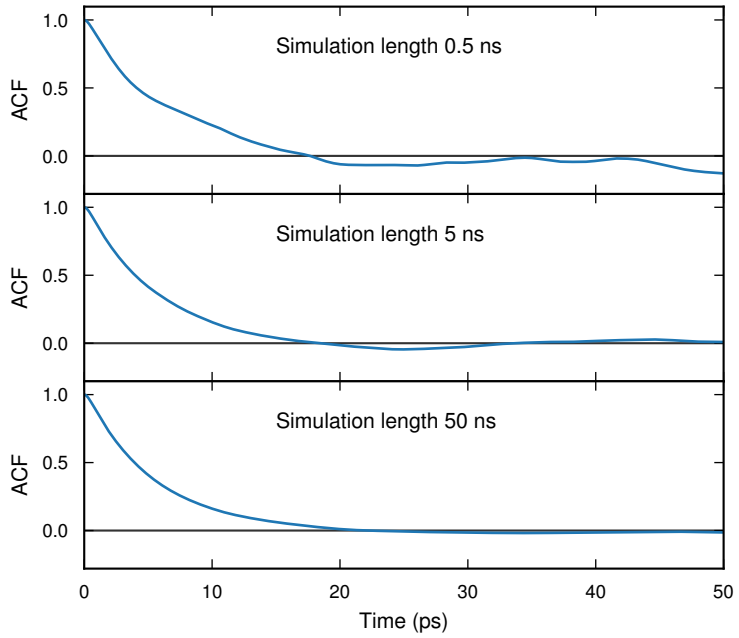

Figure S8: **Auto-correlation functions convergence with respect to simulation length.** The ACF, $C_Q(t)$, of the M-tilt mode at 350 K with different total number of time steps considered in the ensemble averaging. A well converged ACF is obtained for 50 ns.

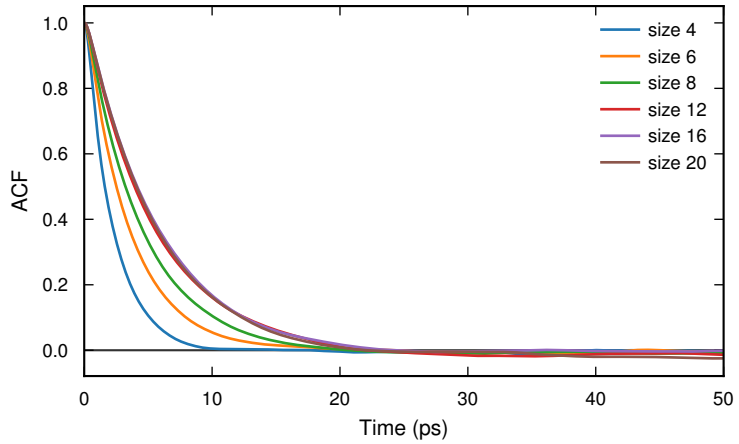

Figure S9: **Auto-correlation functions convergence with respect to system size.** The ACF, $C_Q(t)$, of the M-tilt mode at 350 K for different system size (size N refers to a supercell of $N \times N \times N$ conventional cubic cells). Here, the sizes 12, 16, 20 produce almost identical ACFs.

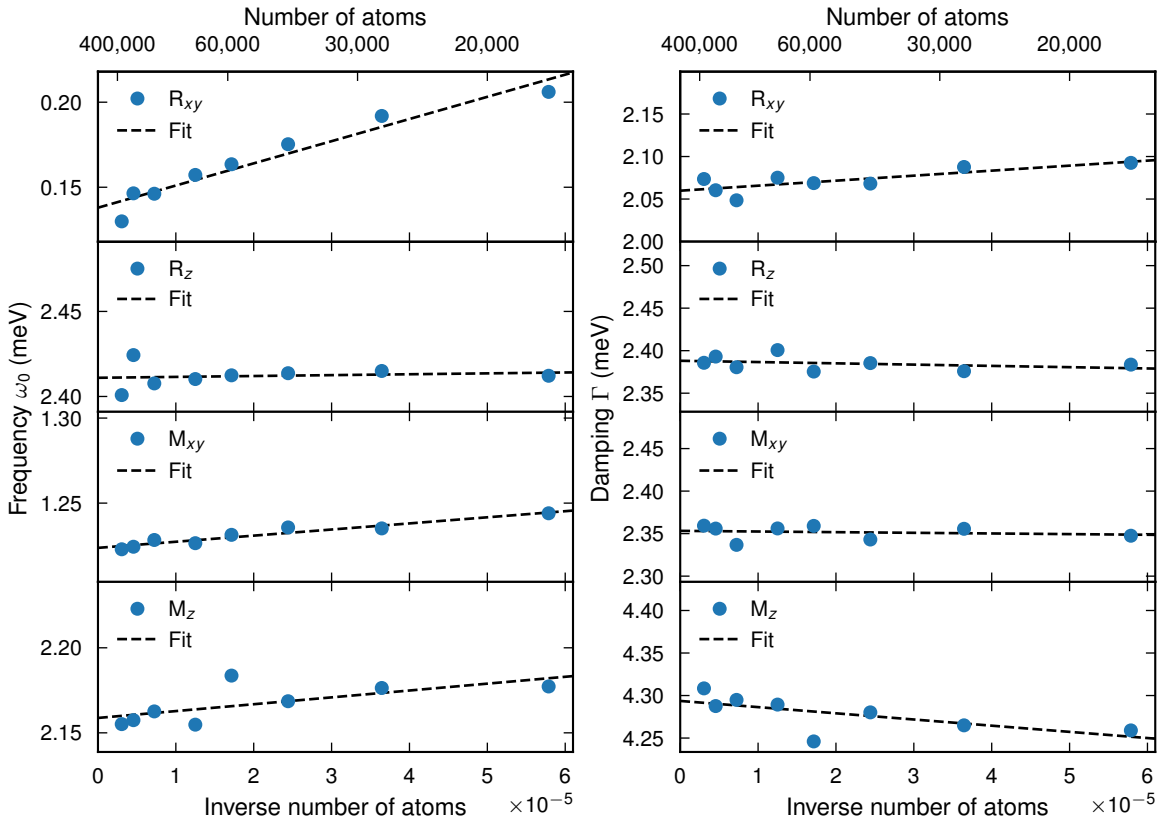

Figure S10: **System size dependency of frequency and damping.** The frequencies, ω_0 and damping, Γ, obtained from fitting the ACFs to a DHO for the different modes in the tetragonal structure for various system sizes at 276 K. The solid lines correspond to linear fits, from which the infinte system size extrapolated values can be extracted. The frequency of the R_{xy} mode shows a strong size dependency, specially for temperatures close to the orthorhombic transition. The dampings, Γ, do not appear to be very sensitive to system size for any temperature.

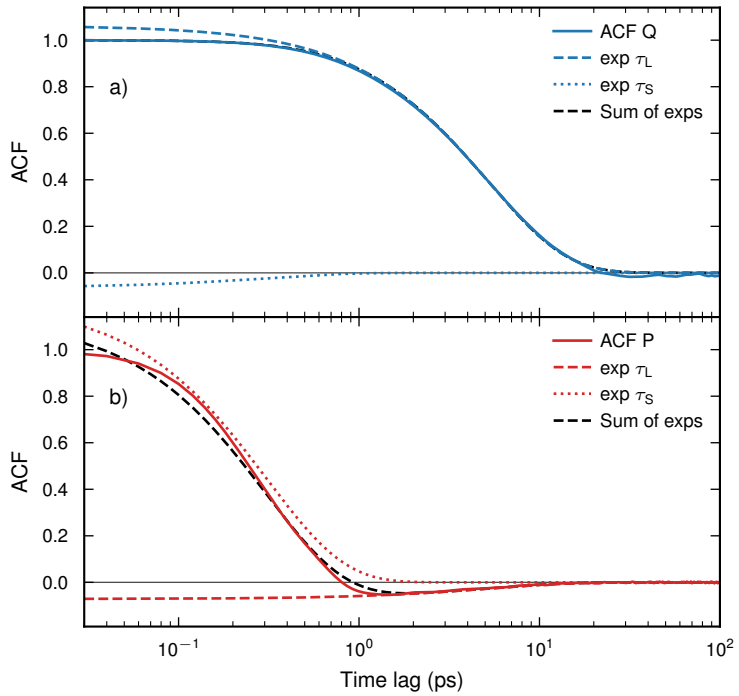

Figure S11: **Decomposition of auto-correlation functions.** (a) The ACF of the mode coordinate, $C_Q(t)$, of the M-tilt mode at 350 K. (b) The ACF of the mode velocity, $C_P(t)$, of the M-tilt mode at 350 K. The timescales are τ_L =5.22 ps and τ_S =0.31 ps. Here, the solid lines corresponds to the raw ACF obtained from MD, the black dashed line corresponds to the fitted DHO, the colored dashed line corresponds to the long-timescale exponential decay in of the overdamped DHO and the dotted line corresponds to the short-time scale exponential decay.

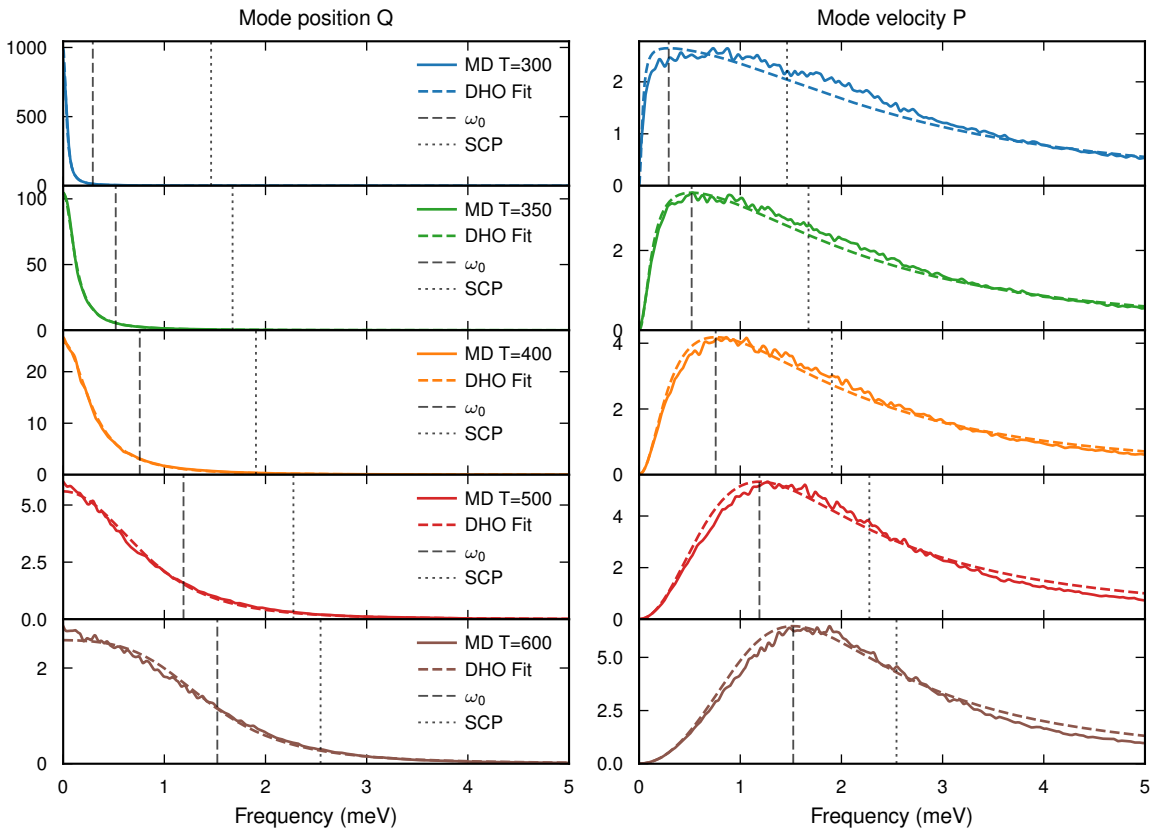

Figure S12: **Phonon mode powerspectra.** Power spectra of the M-tilt mode at various temperatures for the position (Q) and velocity (P) of the mode. The solid lines are the raw spectra obtained from MD simulations, the dashed colored lines correspond to the fits to the DHO, the dashed vertical lines correspond to ω_0 from the DHO and the dotted lines correspond to the frequency obtained from SCP.

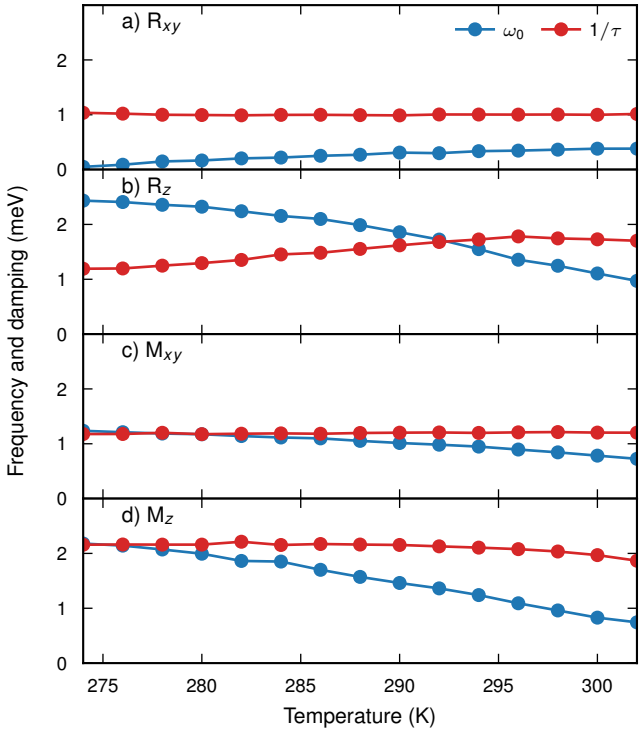

Figure S13: **Phonon frequencies and lifetimes in the tetragonal phase.** Phonon frequencies ω_0 and relaxation time τ in the tetragonal phase obtained from MD simulations for the modes a) R_{xy}, b) R_z, c) M_{xy}, and d) M_z, respectively.

Supplementary Tables

Table S1: Comparison of structural parameters of the orthorhombic, tetragonal and cubic phase between NEP and DFT.

	Spacegroup	Energy (meV/atom)	a (Å)	b (Å)	c (Å)
NEP					
cubic	$Pm\bar{3}m$ (221)	17.589	5.9042		
tetragonal	P4/mbm (127)	4.659	5.7883		5.9791
orthorhombic	Pnma (62)	0.0	5.6388	5.8751	5.9996
DFT (SCAN)					
cubic	$Pm\bar{3}m$ (221)	14.647	5.8987		
tetragonal	P4/mbm (127)	3.753	5.7788		5.9852
orthorhombic	Pnma (62)	0.0	5.7032	5.8682	5.9451

Supplementary References

[1] P. E. Blöchl. Projector augmented-wave method. *Physical Review B*, 50:17953–17979, 1994. doi: 10.1103/PhysRevB.50.17953.

[2] G. Kresse and J. Hafner. Ab initio molecular dynamics for liquid metals. *Physical Review B*, 47: 558–561, Jan 1993. doi: 10.1103/PhysRevB.47.558.

[3] G. Kresse and J. Furthmüller. Efficiency of ab-initio total energy calculations for metals and semiconductors using a plane-wave basis set. *Computational Materials Science*, 6(1):15–50, 1996. doi: 10.1016/0927-0256(96)00008-0.

[4] Jianwei Sun, Adrienn Ruzsinszky, and John P. Perdew. Strongly Constrained and Appropriately Normed Semilocal Density Functional. *Physical Review Letters*, 115:036402, Jul 2015. doi: 10.1103/PhysRevLett.115.036402.

[5] Zheyong Fan, Topi Siro, and Ari Harju. Accelerated molecular dynamics force evaluation on graphics processing units for thermal conductivity calculations. *Computer Physics Communications*, 184(5):1414–1425, 2013. ISSN 0010-4655. doi: doi.org/10.1016/j.cpc.2013.01.008. URL `https://www.sciencedirect.com/science/article/pii/S0010465513000258`.

[6] Zheyong Fan, Zezhu Zeng, Cunzhi Zhang, Yanzhou Wang, Keke Song, Haikuan Dong, Yue Chen, and Tapio Ala-Nissila. Neuroevolution machine learning potentials: Combining high accuracy and low cost in atomistic simulations and application to heat transport. *Physical Review B*, 104: 104309, Sep 2021. doi: 10.1103/PhysRevB.104.104309. URL `https://link.aps.org/doi/10.1103/PhysRevB.104.104309`.

[7] Albert P. Bartók, Risi Kondor, and Gábor Csányi. On representing chemical environments. *Physical Review B*, 87:184115, May 2013. doi: 10.1103/PhysRevB.87.184115. URL `https://link.aps.org/doi/10.1103/PhysRevB.87.184115`.

[8] Zheyong Fan. Improving the accuracy of the neuroevolution machine learning potential for multi-component systems. *Journal of Physics: Condensed Matter*, 34(12):125902, jan 2022. doi: 10.1088/1361-648x/ac462b. URL `https://doi.org/10.1088/1361-648x/ac462b`.

[9] Daan Wierstra, Tom Schaul, Tobias Glasmachers, Yi Sun, Jan Peters, and Jürgen Schmidhuber. Natural evolution strategies. *Journal of Machine Learning Research*, 15(27):949–980, 2014. URL `http://jmlr.org/papers/v15/wierstra14a.html`.

[10] M. Songvilay, N. Giles-Donovan, M. Bari, Z.-G. Ye, J. L. Minns, M. A. Green, Guangyong Xu, P. M. Gehring, K. Schmalzl, W. D. Ratcliff, C. M. Brown, D. Chernyshov, W. van Beek, S. Cochran, and C. Stock. Common acoustic phonon lifetimes in inorganic and hybrid lead halide perovskites. *Physical Review Materials*, 3:093602, Sep 2019. doi: 10.1103/PhysRevMaterials.3.093602. URL `https://link.aps.org/doi/10.1103/PhysRevMaterials.3.093602`.

[11] Tyson Lanigan-Atkins, Xing He, MJ Krogstad, DM Pajerowski, DL Abernathy, Guangyong NMN Xu, Zhijun Xu, D-Y Chung, MG Kanatzidis, Stephana Rosenkranz, R. Osborn, and O. Delaire. Two-dimensional overdamped fluctuations of the soft perovskite lattice in CsPbBr3. *Nature Materials*, 20(7):977–983, 2021. doi: 10.1038/s41563-021-00947-y.

[12] Keivan Esfarjani and Yuan Liang. Thermodynamics of anharmonic lattices from first principles. In *Nanoscale Energy Transport*, 2053-2563, pages 7–1 to 7–35. IOP Publishing, Bristol England, 2020. ISBN 978-0-7503-1738-2. doi: 10.1088/978-0-7503-1738-2ch7. URL `http://dx.doi.org/10.1088/978-0-7503-1738-2ch7`.

[13] T. Tadano, Y. Gohda, and S. Tsuneyuki. Anharmonic force constants extracted from first-principles molecular dynamics: applications to heat transfer simulations. *Journal of Physics: Condensed Matter*, 26(22):225402, 2014. ISSN 0953-8984. doi: 10.1088/0953-8984/26/22/225402.

[14] Lorenzo Monacelli, Raffaello Bianco, Marco Cherubini, Matteo Calandra, Ion Errea, and Francesco Mauri. The stochastic self-consistent harmonic approximation: calculating vibrational properties of materials with full quantum and anharmonic effects. *Journal of Physics: Condensed Matter*, 33(36):363001, jul 2021. doi: 10.1088/1361-648x/ac066b.

[15] Fredrik Eriksson, Erik Fransson, and Paul Erhart. The Hiphive Package for the Extraction of High-Order Force Constants by Machine Learning. *Advanced Theory and Simulations*, 2:1800184, 2019. ISSN 2513-0390. doi: 10.1002/adts.201800184. URL `https://onlinelibrary.wiley.com/doi/abs/10.1002/adts.201800184`.

[16] Olle Hellman, Peter Steneteg, I. A. Abrikosov, and S. I. Simak. Temperature dependent effective potential method for accurate free energy calculations of solids. *Physical Review B*, 87(10):104111, March 2013. doi: 10.1103/PhysRevB.87.104111.